



HAL
open science

Zero-Valent Iron Nanoparticles Supported on Biomass-Derived Porous Carbon for Simultaneous Detection of Cd²⁺ and Pb²⁺

Mohamed Amine Djebbi, Lakhdar Allagui, Mohamed Slim El Ayachi, Saber Boubakri, Nicole Jaffrezic-Renault, Philippe Namour, Abdesslem Ben Haj Amara

► **To cite this version:**

Mohamed Amine Djebbi, Lakhdar Allagui, Mohamed Slim El Ayachi, Saber Boubakri, Nicole Jaffrezic-Renault, et al.. Zero-Valent Iron Nanoparticles Supported on Biomass-Derived Porous Carbon for Simultaneous Detection of Cd²⁺ and Pb²⁺. ACS Applied Nano Materials, 2022, 5 (1), pp.546 - 558. 10.1021/acsanm.1c03333 . hal-03557444

HAL Id: hal-03557444

<https://hal.science/hal-03557444>

Submitted on 17 Feb 2022

HAL is a multi-disciplinary open access archive for the deposit and dissemination of scientific research documents, whether they are published or not. The documents may come from teaching and research institutions in France or abroad, or from public or private research centers.

L'archive ouverte pluridisciplinaire **HAL**, est destinée au dépôt et à la diffusion de documents scientifiques de niveau recherche, publiés ou non, émanant des établissements d'enseignement et de recherche français ou étrangers, des laboratoires publics ou privés.

Zero-Valent Iron Nanoparticles Supported on Biomass-Derived Porous Carbon for Simultaneous Detection of Cd²⁺ and Pb²⁺

Mohamed Amine Djebbi^{1,2,*}, Lakhdar Allagui¹, Mohamed Slim El Ayachi¹, Saber Boubakri³, Nicole Jaffrezic-Renault⁴, Philippe Namour², Abdesslem Ben Haj Amara¹

¹Laboratory of Ressources, Materials & Ecosystem (RME), University of Carthage, Faculty of Sciences of Bizerte, Zarzouna, 7021, Tunisia

²INRAE, UR RiverLy, Centre de Lyon-Villeurbanne, 5 rue de la Doua CS 20244, Villeurbanne, 69625, France

³National Institute for Research and Physico-chemical Analysis, BiotechPole Sidi-Thabet, Ariana, 2020, Tunisia

⁴Institute of Analytical Sciences, University of Lyon, 5 rue de la Doua, Villeurbanne, 69100, France

*Corresponding Author: Mohamed Amine Djebbi

E-mail: med-djebbi@hotmail.fr; mohammed-amine.djebbi@inrae.fr

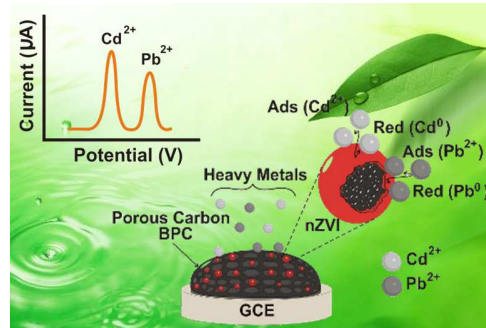
Phone number: (00) 216 27 380 672

Abstract

A Green and efficient electrochemical sensor for simultaneous detection of cadmium (Cd) and lead (Pb) heavy metal ions is proposed in this work. For this aim, biomass-derived porous carbon (BPC) along with zero-valent iron nanoparticles (nZVI) have been used to modify glassy carbon electrodes (GCE). The carbon substrate herein was obtained from abundant marine biomass, *Posidonia oceanica*. The nZVI particles were in-situ reduced on BPC by combining the conventional liquid-phase reduction method of ferric chloride with the impregnating process. The physico-chemical and electroanalytical investigations were established by X-ray diffraction (XRD), Fourier-transform infrared (FT-IR), Raman, X-ray photoelectron (XPS), transmission electron microscopy (TEM), nitrogen adsorption/desorption isotherm, cyclic voltammetry (CV), and electrochemical impedance (EIS), all suggesting that the nZVI particles were successfully anchored and uniformly dispersed on the carbon substrate, and the synergistic effect between the BPC and nZVI properties uplifts the electrocatalytic ability of the modified electrode nZVI-BPC/GCE. The as-fabricated electrode was then assessed and evaluated for the simultaneous detection of Cd²⁺ and Pb²⁺ in an aqueous buffered solution containing acetate using square wave stripping voltammetry (SWSV). Experimental conditions and parameters such as the effect of electrolyte pH, deposition potential, and deposition time for sensing target ions were optimized. Results demonstrated that the sensing electrode exhibited a linear detection range of 2.0–50 µg/L for both metal ions, and detection limits of 0.1926 µg/L and 0.2082 µg/L were recorded for the Cd²⁺ and Pb²⁺, respectively. Moreover, drinking water samples were further analyzed for the practical testing of the developed sensor, where it also revealed adequate detection performances.

Keywords biomass-derived porous carbon (BPC), nanoscale zero-valent iron (nZVI), cadmium (Cd²⁺), lead (Pb²⁺), modified electrode, electrochemical sensor

Graphical abstract



1. Introduction

Certain kinds of water contaminants, such as harmful algal blooms, oil slicks, and plastics that affect watersheds and aquifers, are often in sight. However, other pollutants are not so readily apparent, they dissolve easily, which makes their effects potentially more dangerous. Among them, heavy metals presented the greatest threat for the environment¹⁻³. Draining into water sources from mining and smelting operations, industrial production sites, or from natural atmospheric deposition, these elements can reach taps worldwide. Heavy metals not only are unable to biodegrade but also tend to accumulate in body organs and tissues, which thereby represents a serious danger to human health according to the World Health Organization (WHO)^{4,5}, even in trace levels. Lead (Pb) and cadmium (Cd) are examples of toxicant metals, originating from industrial emissions, that showed a worrying increase through the aquatic biosphere, and which have been recognized as potential hazards to human safety⁶⁻⁸. Lead is typically used in petroleum refining (over 50% of emissions)⁵, it is a potent neurotoxin and suspected carcinogen that can cause harm to the brain, red blood cells, lung disease, and kidney problems^{9,10}. WHO established that the limit of Pb in drinking water is 10 ppb^{9,11}. On the other hand, cadmium is widely recognized as one of the most toxic and harmful heavy metals, which originates from electroplating industries². It is harmful to the kidneys, bones, and respiratory system, and is suspected of being a carcinogenic and an endocrine disruptor². Trace levels of cadmium can substantially magnify the carcinogenic potency by inhibiting the ability to change the genetic material (DNA)¹². The permitted concentration level of Cd in drinking water set by WHO is about 3 ppb^{13,14}.

Therefore, developing simple and reliable methods for the safe detection and careful monitoring of these toxic metal ions in water is of paramount importance. For now, the accurate and robust measurement options of Cd²⁺ and Pb²⁺ invokes the deployment of expensive pieces of equipment and facilities, including atomic-absorption and atomic-emission spectrophotometry, mass spectrometry, inductively-coupled-plasma mass spectrometry, X-ray fluorescence spectrometry, and high-performance liquid chromatography, etc^{9,15-17}. Although these methods are characterized with high sensitivity, specificity, and high resolution, they are time-consuming, bulky instrumentation, exhibit high operational cost, and can be performed only in accredited laboratories. Thus, the focus on developing portable, accurate, fast, user-friendly, and low-cost devices is required for point-of-care detection. Recently, electrochemical sensors have gained increasing attention for detecting metal ions into a water source owing to their simpler approach, low cost, fast response, compatibility for miniaturization, and ease of assembly and adaptability to be integrated into portable devices^{18,19}. They may, however, present great advantages in detecting the target analytes in complex systems with low limits of detection (LOD) and high sensitivity²⁰. Particularly, stripping voltammetry is a competent electroanalytical technique that consists in enabling many chemical reaction processes to provide electrochemical signals of target probe binding in real-time and offers the possibility of

analyzing several trace metal ions simultaneously with ultrahigh sensitivity and excellent selectivity.

However, the electrochemical response of a such target analyte depends on the nature of the transducer surface that constitutes the detection platform. Along this line, glassy carbon-based-electrode (GCE) transducers are widely used in sensing research of trace metal ions analysis due to their high conductivity, good biocompatibility, wide potential range, and easy chemical surface modification^{15,21}, which give the sensor an outstanding sensitivity and selectivity. Previously, many works have initiated the electrode-surface modification to improve the surface-area-to-volume ratio and boost the rate of electron transfer and hence enhance the sensitivity, selectivity, reproducibility, and stability of the electrode^{6,15,21-25}.

Aiming at developing high-performance electrode materials and providing more sensitive electroanalysis, nanoscale zero-valent iron (nZVI) structures are the focal point of this work. nZVI is a core-shell structure (Scheme 1), which is very often explored for adsorption and uptake of toxic metal ions, due to its unique properties of the surface layer such as the high reducing ability and the high surface activity^{5,26,27}. The surface layer of nZVI consists of negatively charged iron oxides and iron hydroxides layer, which provides the structure high-density sites for the detection of metal ions likely through correlated mechanisms including adsorption (via complexation) and electron transport process, while the metallic iron core act as an electron donor that promotes the rapid reduction and enrichment of the heavy metal ion^{5,28}. Indeed, the reduction of NZVI-based materials for the heavy metals involves two distinct pathways:²⁷ (i) direct reduction of heavy metal by Fe⁰ core; (ii) primary adsorption of the heavy metal on the shell and then a gradual reduction in the adsorbed metal by the Fe⁰ core.

However, despite the prominent properties of nZVI, two major challenges limit its optimum performance and efficiency:²⁹ (i) oxidation and (ii) strong propensity for aggregation. To overcome these issues, loading and embedding nZVI particles on the surface of a template would extend their lifetime and effectively suppress their aggregation and oxidation. For this, biomass-derived porous carbon (BPC) is considered to be an ideal stabilizer and suitable material for dispersing nano iron particles due to its wide abundance and ecological role, as well as its structural, chemical, and thermal stability^{8,24,30-33}. Earlier research conducted by Chen et al.,³⁴ and Song et al.,³⁵ have shown that the carbon network could increase the reactivity of the iron particles through the Fe/C cross-link and thus increase the detection efficiency of heavy metal ions. In addition to the above, the BPC material exhibits a large surface area and relatively good electrical conductivity which are considered as paramount properties for the electrode modifiers in sensing applications^{8,24}. Benefiting from the synergy between the hierarchically

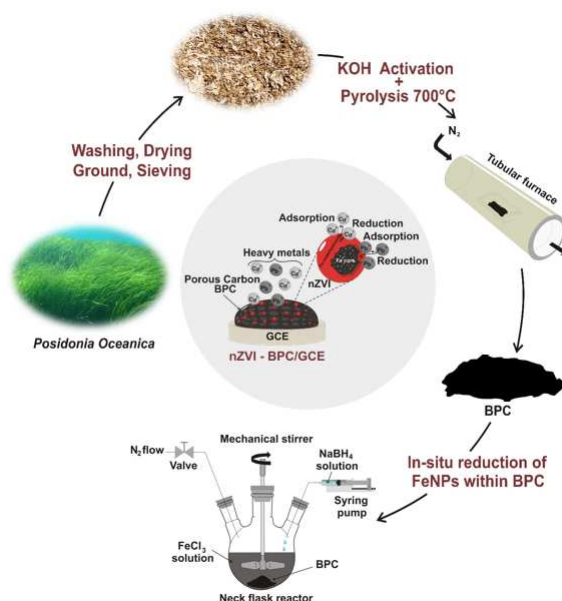
Scheme 1. The schematic core-shell structure of nZVI.



porous framework of the BPC and the strong adsorption ability or the electrocatalytic activity of the nZVI particles, the nZVI-BPC nanocomposite can thus supply more active sites for electrode reactions, accelerate the electron transfer between the active species and electrode, and improve the signal-to-noise ratio, which all contribute to enhancing the sensor's detection limit against the toxic metal ions.

Herein, we report a simple and effective synthesis way for the preparation of nZVI particles loaded BPC (Scheme 2). *Posidonia oceanica* marine biomass was employed as a carbon source to prepare the porous carbon materials (BPC) following the thermal carbonization process, then nZVI particles were randomly and uniformly embedded into the carbon network by combining the impregnation-reduction method of ferrous ions by NaBH₄. The physico-chemical features of the nZVI-BPC nanocomposite were investigated by X-ray diffraction (XRD), Fourier-transform infrared (FT-IR), Raman, and X-ray photoelectron (XPS) spectroscopies, transmission electron microscopy (TEM), and nitrogen adsorption/desorption isotherm. Next, the so prepared nanocomposite was used to modify GCE via the drop-casting technique, characterized by cyclic voltammetry (CV) and electrochemical impedance spectroscopy (EIS), and subsequently utilized towards the detection of Cd²⁺ and Pb²⁺ ions in pH 5.0 acetate buffer solution using the square wave stripping voltammetry (SWSV) method. It is shown that the nZVI-BPC/GCE exhibits excellent sensitivity, high reproducibility, and good stability, and should be highly praised as a practical and cost-effective heavy metal sensor for monitoring drinking water quality. As far as we know, there is no report to date describing the electrochemical detection of heavy metal ions by using a such composite precursor.

Scheme 2. Schematic representation of the step-wise fabrication of the Cd²⁺ and Pb²⁺ heavy-metal-sensor.



2. Experimental section

2.1. Materials and equipment

The tools used in this work are as follows: a Sartorius BCE224-1S electronic balance, Memmert vacuum drying oven, Nabertherm RT331CAN furnace, DU-45 ultrasonic bath sonicator, pyrex beakers, neck flask reactor, eppendorf pipette, rotating glassy carbon electrode, Razel syringe-pump system, α -pH1000 Eutech Instruments, GFL distillers 2104, Velp Scientifica magnetic stirrer, and Rod mechanical stirrer were used in the study.

2.2. Chemicals and reagents

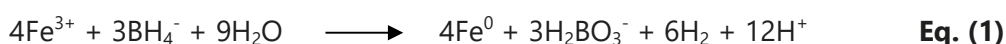
The main chemicals and reagents were as follows: iron(III) chloride (FeCl_3 , MW: 162.20, 97%), sodium borohydride (NaBH_4 , MW: 37.83, $\geq 98\%$), lead(II) nitrate ($\text{Pb}(\text{NO}_3)_2$, MW: 331.21, $\geq 99\%$), cadmium(II) nitrate tetrahydrate ($\text{Cd}(\text{NO}_3)_2 \cdot 4\text{H}_2\text{O}$, MW: 308.48, 98%), potassium ferrocyanide(II) trihydrate ($\text{K}_4\text{Fe}(\text{CN})_6 \cdot 3\text{H}_2\text{O}$, MW: 422.39, 98.5-102.0%), potassium hexacyanoferrate(III) ($\text{K}_3\text{Fe}(\text{CN})_6$, MW: 329.24, $\geq 99\%$), potassium hydroxide (KOH, MW: 56.11, $\geq 85\%$), hydrochloric acid (HCl, MW: 36.46, 37%), ethanol ($\text{CH}_3\text{CH}_2\text{OH}$, MW: 46.07, 96.0-97.2%) were analytically pure grades, purchased from Sigma-Aldrich and used directly without any further purification. The supporting electrolyte solution used in all experiments was 0.1 M acetate buffer (ABS, pH 5.0). All solutions were prepared by using distilled water.

2.3. Synthesis of nZVI-BPC nanocomposite

For the preparation of the carbon materials, *P. oceanica* biomass waste was collected from a local beach in the province of Bizerte (Mediterranean coast to northern Tunisia). Typically, the biomass was firstly washed using distilled water with ultrasonic-assisted treatment to remove sand grains and undesirable impurities. Subsequently, the obtained grass was sun-dried for 2 days, mixed, ground, and sieved to yield the finest and homogenous powders, and then soaked in KOH solution while stirring under nitrogen flow for about 24 h. Consequently, the activated powdered material was systematically dried at 100° C for 24 h and then undergoes a carbonization process at 700° C with a heating rate of 5° C for 3 h in an N_2 flow tubular furnace, followed by washing cycles with a dilute HCl (1 M) and distilled water until neutral and dried in vacuum at 100° C overnight. The final product so obtained was denoted as BPC.

Later, nZVI particles were in-situ synthesized onto the BPC substrate following the known liquid-phase reduction method (Eq. 1) and the impregnation process³⁶. In brief, 4.84 g of ferrous chloride was dissolved in a 100 mL liquid form consisting of a mixture of 70% (v) distilled water and 30% (v) ethanol with thorough stirring for 1 h at 60° C on a mechanical stirrer, under N_2 atmosphere. The obtained solution was then followed by impregnation of 0.5 g BPC for another 60 min in an ultrasonic bath. Next, 50 mL of NaBH_4 solution (1 M) was added dropwise under vigorous stirring into the ferrous solution at a flow rate of 0.12 mL/min using the Razel syringe-

pump system. Once the sodium borohydride (NaBH₄) addition was completed, the mixture was further stirred for another 30 min while being maintained under a constant N₂ flow and the resulting product was then collected by centrifugation, washed thoroughly with distilled water and ethanol, and finally dried at 60° C overnight. The final solid sample was stored in a vacuum desiccator and labeled as nZVI-BPC.



2.4. Physico-chemical characterizations

The crystalline structure and phase purity of samples were investigated using X-ray diffractometry (XRD). XRD patterns were acquired in ambient air on a Bruker AXS D8 Advance with CuK α radiation source ($\lambda = 1.5406 \text{ \AA}$). The instrument operates at 40 kV and 30 mA, with continuous scanning from 3.5 to 60°, in the step of 0.02° and 57,70 s counting time per step. The chemical groups were examined by Fourier transform infrared spectrophotometer (FTIR, Nicolet 200). Scans were collected in transmittance mode in the scanning range of 4000-500 cm⁻¹ with a resolution of 1 cm⁻¹ at room temperature and the samples were ground and mixed thoroughly with KBr. Raman analysis was carried out on a Laser Raman spectrophotometer (Renishaw InVia Reflex RM3000), operating at room temperature with an emission wavelength of 532.0 nm in backscattering geometry. The morphology of the samples was visualized by transmission electron microscopy (TEM). TEM graphs were taken using a Tecnai G2 FEI microscope, operating at an accelerating voltage of 200 kV. The textural information, including the specific surface area, total pore volume, and mean pore size, were analyzed by nitrogen adsorption/desorption measurements at 77 K, carried out with ASAP 2020 Plus Physisorption Analyzer from Micromeritics Instrument Corporation. The surface composition and chemical state were analyzed using X-ray photoelectron spectroscopy (XPS, VG Escalab220iXL instrument) equipped with an Mg polychromatic radiation (MgK $\alpha = 1253.6 \text{ eV}$) as the excitation source.

2.5. Preparation of nZVI-BPC/GCE

Before preparing the modified electrode, a pre-treatment step was initially applied to the GCE to remove surface dirt and impurity and also to improve its kinetics to achieve accurate and reproducible measurement results. It consists of ultrasonically cleaning the GCE with ethanol and distilled water for at least 20 min and polishing it by using sandpaper and 0.5 nm alumina slurry³⁷. The polished GCE was then rinsed with ethanol and placed in distilled water for 5 min and finally dried at ambient temperature. Next, 5 mg of nZVI-BPC nanocomposite was dispersed in 1 mL of aqueous ethanol 70% (v/v), treated in a sonicator for 1 h, and later, 5 μL of the dispersion was withdrawn and dripped onto the surface of the smooth and polished GCE, followed by drying at 60° C for 1h.

2.6. Electroanalytical measurements

All the electrochemical measurements in this work were conducted on an electrochemical analyzer (Autolab PGSTAT302N) workstation driven by Nova software, using a conventional three-electrode cell. A bare GCE (\varnothing 3 mm) or modified GCE serves as a working electrode; platinum (Pt, \varnothing 0.5 mm) wire as an auxiliary electrode, and saturated calomel electrode (SCE) as a reference electrode. The electrocatalytic activity of the modified electrode was examined through cyclic voltammetry (CV) and electrochemical impedance spectroscopy (EIS) in 10 mM of $[\text{Fe}(\text{CN})_6]^{3-/4-}$ redox couple as a probe solution. CV curves were recorded from -600 mV to 600 mV at the following scan rates 50, 100, 150, 200, 250, 300 mV/s and EIS Nyquist plots were performed in the frequency range from 100 mHz to 100 kHz with a 10 mV ac input and riding dc potential of 200 mV. The analytical performances of the modified electrode towards Cd^{2+} and Pb^{2+} detection were evaluated using square wave voltammetry (SWSV) in stripping mode, in 0.1 M acetate buffer solution (ABS, pH 5.0) in the potential range from -1.0 V to -0.4 V. The SWSV measurements were performed as follows: step potential of 5 mV, frequency of 25 Hz and amplitude of 20 mV. The experimental conditions such as the effect of pH, deposition potential, and deposition time for sensing target ions were also explored and optimized. Before each run of the experiment, a desorption scan of 0.3 V for 60 s was applied to the modified electrode in a blank solution to eliminate the residual metal ions from the previous measurement under stirring conditions.

3. Results and discussion

3.1. Sample characterizations

The crystalline structures of BPC and nZVI-BPC were investigated using XRD analysis (Figure 1A). As shown in Figure 1A, two broad diffraction peaks are observed at 2θ values of approximately 23.2° and 40.7° in the XRD pattern of BPC, which can be indexed to the (002) and (100) diffraction planes of the carbon atoms layers arranged in a hexagonal lattice⁶. The wide peak at around 40.7° indicates a higher degree of graphitization in the carbon structure after the KOH etching. While upon incorporating nZVI onto the BPC substrate, two additional peaks have appeared at a 2θ angle of 31.9° and 46.2° correspond to the (311) and (110) indexed planes of nZVI, respectively. The one at 46.2° is typical of pure $\alpha\text{-Fe}^0$ crystal³⁶. However, the diffraction peak at 31.9° is attributed to the iron oxides ($\text{Fe}_2\text{O}_3/\text{Fe}_3\text{O}_4$), produced from the decomposition of ferric chloride. Hence, the XRD analysis demonstrates that nZVI has a specific core-shell structure with a metallic core of zero-valent iron surrounded by a passivated thin shell of iron oxides. Moreover, the d-spacing (d_{002}) of the BPC crystallites decreased from 0.374 to 0.352 nm, which demonstrates the successful incorporation and homogenous growth of nZVI particles onto the BPC substrate. Further analysis by using the Sherrer calculator in the X'Pert HighScore Plus software based on the (110) reflection peak revealed an average crystallite size of 5 nm for the Fe^0 particles, confirming the nanoscale properties of nZVI particles.

The path through which nZVI particles were embedded onto the BPC substrate was also studied by FT-IR spectroscopy in the scanning range between 500 and 4000 cm^{-1} . Figure 1B shows the FT-IR spectra of BPC and nZVI-BPC samples. As shown in Figure 1B, the BPC support exhibited characteristic absorption peaks of activated porous carbon appeared at 3431, 2920, 1629, 1507, 1387, and 1098 cm^{-1} ³⁸. The wide peak observed at 3431 cm^{-1} can be assigned to the O–H stretching bond vibration of hydroxyl groups deduced from both KOH etching and absorbed water, while that of 2920 cm^{-1} is assigned to the C–H stretching bond vibration. The bond at 1629 cm^{-1} is due to the stretching vibration of carbonyl groups (C=O) and the bond around 1507 cm^{-1} may be attributed to the skeletal vibration of C=C in aromatic rings. The absorption peak occurred at 1387 cm^{-1} suggests the presence of aliphatics and the band that appeared at 1098 cm^{-1} is probably resulting from C–O stretching vibrations. Meanwhile, BPC-nZVI revealed three additional peaks centering at around 613, 1019, and 2360 cm^{-1} , which could correspond to the Fe–O stretch associated with the iron oxides ($\text{Fe}_2\text{O}_3/\text{Fe}_3\text{O}_4$) shell surrounding the Fe^0 core. On the other hand, the O–H bond of the hydroxyl groups has shifted from 3431 to 3398 cm^{-1} and broadened, suggesting therefore that the nZVI particles are successfully loaded onto the BPC surface.

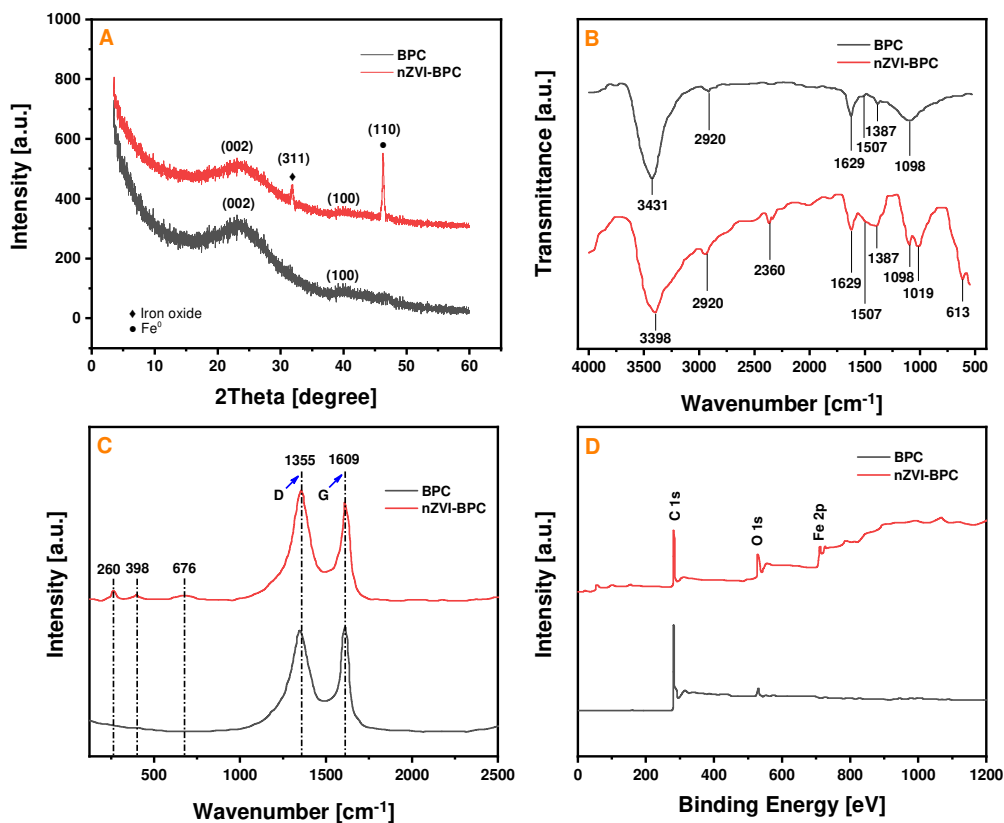


Figure 1. (A) XRD pattern, (B) FT-IR spectra, (C) Raman spectra, and (D) XPS spectra of BPC template and nZVI-BPC nanocomposite.

The outcomes described above are consistent with the analysis in conjunction with Raman spectroscopy. In fact, the Raman analysis of BPC and nZVI-BPC samples revealed the presence of two noticeable peaks centering at 1355 (D-band) and 1609 (G-band) cm^{-1} (Figure 1C), which may be attributed to the defects in the disordered carbon structure and the sp^2 graphitized carbons, respectively³⁹. Both of the bands suggest an ideal graphitic structure, which would enhance the electrochemical performance in the sensing application. Accordingly, the D to G band intensity ratio (I_D/I_G) provides a piece of information on the crystalline structure of the graphitic carbon and usually allows access to the graphitization degree of carbon materials⁴⁰. In the case of the BPC sample, the I_D/I_G ratio was about 0.98, however, this ratio was negligibly changed for the nZVI-BPC (1.02) compared to the BPC, indicating that the carbon lattice still retains a perfect graphitic structure even after embedding nZVI particles. Furthermore, three Raman bands were also observed in the nZVI-BPC spectrum at around 260, 398, and 676 cm^{-1} ³³, which are expected to be ascribed to the Fe–O stretching vibration.

The chemical states analysis of the BPC and nZVI-BPC were investigated by XPS measurements (Figure 1D). As observed in Figure 1D, the XPS analysis spectra demonstrate the presence of C and O elements on the BPC surface and C, O, and Fe on the composite surface. The BPC template exhibited two peaks that appeared at 284.6 and 533.3 eV, which are directly related to the binding energies of C1s and O1s, respectively. While the nZVI-BPC spectrum exhibited an additional peak at 710.6 eV, attributed to the binding energy of Fe2p, which confirms that the FeCl_2 was composed into Fe^0 nanoparticles, and irons with surrounded oxidized shells were anchored onto the BPC support. Besides, the peak intensity of C1s is reduced after loading nZVI onto the BPC surface, which might be explained by the homogenous dispersion of nZVI particles onto the carbon precursor. Contrary to C1s, the peak intensity of O1s is increased upon anchoring the iron particles, which may be related to the unavoidable adsorbed oxygen species and/or the slight oxidation of the Fe^0 core. This is beneficial in providing and exposing more active sites and is responsible for the enhancement in the electrocatalytic ability. Overall, all those peaks and changes are in good correspondence and identical to the results obtained in the previous reports^{33,35}.

TEM was also employed for the inspection of morphology and microstructure of the as-prepared BPC and nZVI-BPC materials (Figure 2). Figure 2A provides details on the BPC structure. The irregular and layered microstructure can be observed at the edge of a fracture referred to as "feathered edge", resulting from the random stacking of sp^2 -bonded carbon sheets. Moreover, atom-thick carbon sheets are set with substantial quantities of dark and white spots between the disordered carbon layers, which suggests that abundant micropores and mesopores exist in the BPC lattice and these pores are expected to give enough sites, thereby maximizing the electroactive surface area where nZVI can be anchored. No lattice distance can be discerned in the graph, which further reveals the highly-disordered microstructure of the as-synthesized porous carbon. Meanwhile, the TEM image of nZVI-BPC (Figure 2B) shows the

presence of dark and uniformly dispersed nanospheres shape on the carbon matrix in size of 5-20 nm that corresponds to the nZVI nanoparticles.

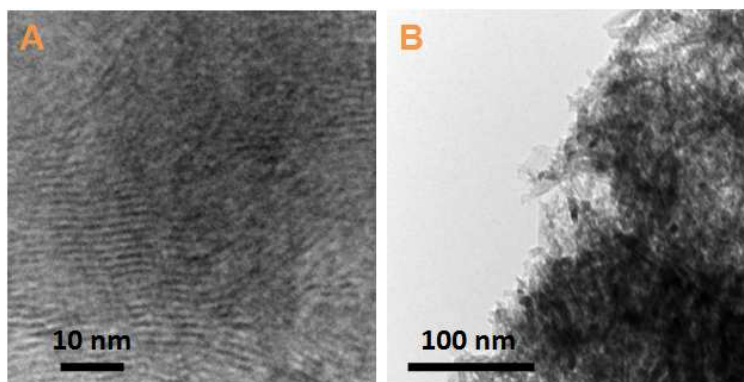


Figure 2. TEM graphs of (A) BPC matrix and (B) nZVI-BPC nanocomposite.

Furthermore, N_2 adsorption/desorption measurements were made to investigate the surface porosity of BPC and nZVI-BPC, and the isotherm branch and pore size distribution plots are shown in Figure S1. Figure S1A shows the isotherms of the samples, both BPC matrix and nZVI-BPC nanocomposite revealed similar profile and exhibited the emblematic type IV isotherm according to the IUPAC classification of isotherms. The existence of hysteresis loops extending in the relative P/P_0 range between 0.28 and 0.97 together with the steep increase in the N_2 gas uptake at the relatively low-pressure region ($P/P_0 < 0.05$) suggests the microporous and mesoporous nature of the samples. Furthermore, the corresponding pore size distribution patterns of the BPC and nZVI-BPC nanocomposite also confirm the co-existence of both micro- and mesoporosities in the samples (Figure S1B). The quantitative textural parameters, including the specific surface area and pore analysis of the samples, are listed in Table S1. BPC matrix had a specific surface area of $752.58 \text{ m}^2/\text{g}$, total pore volume of $0.091 \text{ cm}^3/\text{g}$, and average pore size of 4.16 nm , providing ample site for embedding nZVI particles. Upon loading the BPC surface with nZVI, the surface area, pore volume, and pore size distribution decreased to $680.91 \text{ m}^2/\text{g}$, $0.080 \text{ cm}^3/\text{g}$, and 3.51 nm , respectively. This decrease in the textural parameters of the nanocomposite suggests the successful integration and the improvement of the dispersibility of nZVI particles into the distorted and disordered graphitized carbon layers, which caused blockage of surface pore sites on the carbon matrix and, consequently the decrease in pore size. However, it is noteworthy that the porous structure of the BPC is well maintained even after the nZVI loading, which is beneficial for a higher mass transfer process on the electrode surface.

3.2. Electrochemical characterization of the sensor

To explore the sensor ability, the electrochemical properties of the stepwise modification of GCE were investigated using CV and EIS measurements in $10 \text{ mM } [\text{Fe}(\text{CN})_6]^{3-/4-}$ redox probe solution. The results are shown in Figure 3. Figure 3A shows the cyclic voltammograms of bare GCE,

BPC/GCE, and nZVI-BPC/GCE performed in the potential window from -600 to 600 mV vs SCE with a scan rate of 50 mV/s. As indicated in Figure 3A, the graphical analysis shows a pair of redox peaks, which belong to the oxidation and reduction reactions of Fe^{2+} to Fe^{3+} and Fe^{3+} to Fe^{2+} , respectively, predicting the electron transfer dynamics between the negatively-charged redox probe and the electrode surface. On BPC/GCE, the redox peaks increased slightly with an increase in the peak-to-peak potential separation owing to its enlarged conductive surface area. However, the peak currents were greatly enhanced on nZVI-BPC/GCE, and the peak-to-peak separation diminished. Therefore, the presence of nZVI-BPC on the electrode surface can substantially improve the electrochemical responses because of the excellent electrocatalytic activity of the nZVI nanoparticles. Electrochemical parameters of CV curves for GCE bare, BPC/GCE, and nZVI-BPC/GCE are listed in Table S2. As seen in Table S2, the maximum oxidation and reduction currents of nZVI-BPC/GCE are 1.30 and 0.97 mA, which are 0.34 and 0.38 mA higher than those of GCE, respectively, and the peak potential separation (ΔE_p) is 141.09 mV lower than that of GCE. These results nonetheless indicate that the nZVI-BPC nanocomposite increased the electroactive surface area and improved the electron transfer process, which may offer preferred electrochemical heavy metals detection.

Figure 3B shows the Nyquist plots of GCE bare, BPC/GCE, and nZVI-BPC/GCE recorded at a constant applied voltage of 200 mV. As seen, the whole plot revealed a similar trend. Semicircles at the high to medium frequencies region were observed, corresponding to the capacitive behavior of the electrode⁴¹. The measurement of the semicircle diameter in the Nyquist plots allows us to estimate the value of the ohmic or solution resistance (R_s) and charge transfer resistance (R_{ct}). The ohmic resistance and charge transfer resistance are commonly used to access the electrochemical kinetics occurring at the interface between an electrode and an electrolyte solution. The ohmic resistance consists of contact, electrode, and solution resistance, and directly reflects the conductivity of the electrode. Whereas the charge transfer resistance arises from the interface between the electrolyte and electrode, and its value is associated with the probe kinetics. By fitting the data of the Nyquist plots using the simple Randles circuit [$R_s(C_{dl}R_{ct})$] (inset of Figure 3B, where R_s and R_{ct} represent the ohmic resistance of the electrolyte solution and the charge transfer resistance, respectively, while C_{dl} is the double layer capacitance), the calculated R_{ct} and R_s values are listed in Table S2. There is a slightly decrease in the R_{ct} and R_s when the GCE is coated with BPC, where $R_{ct} = 14.08 \text{ kohm.cm}^2$ and $R_s = 16.93 \text{ ohm.cm}^2$ for GCE, and 13.69 kohm.cm^2 and 14.35 ohm.cm^2 for BPC/GCE, respectively. This decrease in R_{ct} and R_s occurs due to the good electrical conductivity and large surface area of the BPC with respect to the GCE. Upon the addition of nZVI into BPC, a further decrease in the R_{ct} and R_s values was observed in the nZVI-BPC nanocomposite. The semicircle domain with R_{ct} and R_s values can be estimated to be 11.75 kohm.cm^2 and 5.33 ohm.cm^2 , respectively. This significant decrease in resistances indicates that the nZVI particles behaved as a good conductor, which accelerated the electron transfer, increased the electrical conductivity on BPC

and thereby enhanced the electrocatalysis by the nZVI-BPC/GCE. These findings are also in line with those obtained by the voltammetric measurements (Figure 3B).

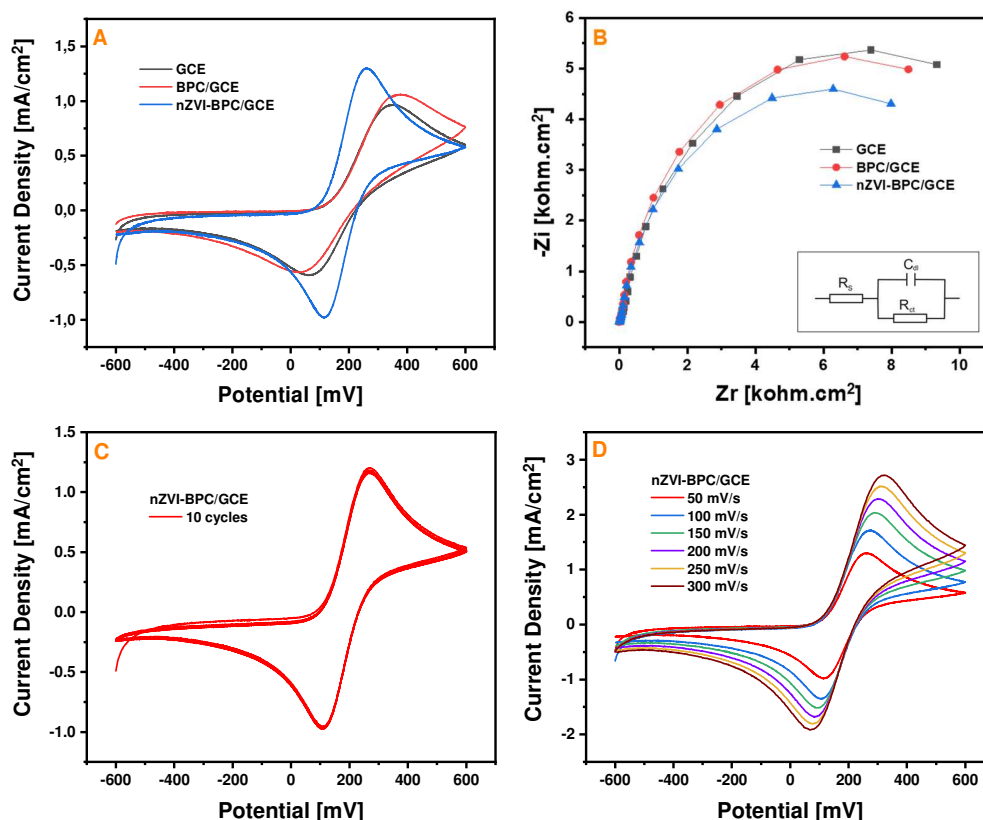


Figure 3. (A) CV curves and (B) EIS Nyquist plots of GCE bare, BPC/GCE, and nZVI-BPC/GCE; (C) 10 CV cycles and (D) effect of CV scan rate of nZVI-BPC/GCE, in 10 mM $[\text{Fe}(\text{CN})_6]^{3-/4-}$ redox probe solution.

To further study the electrochemical stability of nZVI-BPC/GCE, successive CV scans at the scanning rate of 50 mV/s within the range between -600 and 600 mV were carried out. Figure 3C shows the cyclic voltammetry of nZVI-BPC/GCE over 10 cycles. The cycling measurements exhibited diminutive or negligible deterioration from the first scan up to the tenth scan, which suggests that the as-fabricated sensor showed excellent stability. In addition, the effect of the varying scan rates was tested in the range of 50–300 mV. Figure 3D shows CV curves for nZVI-BPC/GCE with increasing scan rates of 50, 100, 150, 200, 250, and 300 mV/s. The integrity of the CV curves behave similarly and show well-defined redox peaks. However, the current peaks show an upward trend in regular gradient slopes with rising scan rates, and there is no glaring shift between the potential peaks, thus indicating that the reaction on the electrode surface is an approximately reversible process and also invoking that the redox species adsorb onto the electrode surface before electron transfer⁴².

3.3. Electroanalytical response for Cd^{2+} and Pb^{2+} detection

3.3.1. Optimization of SWSV parameters

To explore the sensitivity of the sensor for the simultaneous detection of Cd^{2+} and Pb^{2+} , the stripping voltammetry technique was used to investigate the electrochemical response of the heavy metals. Figure 4A shows the SWSV of 50 $\mu\text{g/L}$ Cd^{2+} and Pb^{2+} ions in 0.1 M ABS on GCE bare, BPC/GCE, and nZVI-BPC/GCE. As shown in Figure 4A, two well-separated SWV peaks are observed at approximately -0.77 and -0.54 V with GCE, around -0.79 and -0.52 V for BPC/GCE, and into -0.78 and -0.53 for nZVI-BPC/GCE, accountable to Cd^{2+} and Pb^{2+} , respectively. The peak separation between Cd^{2+} and Pb^{2+} was broad enough to discriminate Cd^{2+} and Pb^{2+} individually and simultaneously. Furthermore, Figure 4A shows that BPC/GCE outperforms the GCE bare in terms of the stripping peak current responses, due to the hierarchically porous structure of the carbon substrate, which improves the chelating and adsorption capacity of metal ions, resulting in faster diffusion and better detection performance. However, much higher peak currents were obtained with the nZVI-BPC/GCE compared to those recorded with GCE bare and BPC/GCE, thanks to the electroreduction ability and good intrinsic conductivity of the nZVI particles, which results in better sensitivity. When nanoscale iron particles are exposed to water media, they interact with water and oxygen to form an external surface of iron (hydr)oxide hydrate, thereby providing sites for the adsorption of heavy metals. The reduction of metal, herein, involved two pathways (Scheme 3): (i) the heavy metal is first adsorbed onto the iron oxide shell of nZVI and then (ii) followed by its continuous reduction by the Fe^0 core in the following reaction: Cd^{2+} or $\text{Pb}^{2+} + \text{Fe}^0(\text{s}) \rightarrow \text{Fe}^{2+} + \text{Cd}^0(\text{s})$ or $\text{Pb}^0(\text{s})$. Hence, the sensing improved performance is part of the associated synergy between the porous template of BPC and nZVI particles, where nZVI could serve as an excellent electron donor for the reduction of the metallic ions, offering thus an adequate electrocatalytic activity and an admirable electrochemical surface with more abundant anchor sites for the uptake of heavy metal ions.

To get the maximum sensitivity of the nZVI-BPC/GCE for the detection of 50 $\mu\text{g/L}$ Cd^{2+} and Pb^{2+} ions, various analytical parameters, including electrolyte pH, deposition potential, and deposition time were optimized sequentially in 0.1 M ABS. The obtained results are shown in Figure 4. Figure 4B displays the investigation results for the effect of solution pH on the determination of Cd^{2+} and Pb^{2+} ions over the range of 3.0–7.0. As depicted in Figure 4B, the peak currents were weak at pH 3.0 and then increased tremendously to reach a maximum value at pH 5.0. Beyond the pH value of 5.0, the current responses decreased up to pH 7.0. Consequently, the pH 5.0 was set as the optimal pH in the subsequent experiments. This phenomenon might be attributed to the influence of the pH buffer on the reactivity of the nZVI particles. In a lower acidic medium, the metal ions uptake is low due to the formation of iron complex species $[\text{Fe}(\text{H}_2\text{O})_6]^{2+}$ with the seemingly slow hydroxyl radical production. Meanwhile, in higher pH values, the detection rate declined, which can be related to the following factors: (i) the formation of relatively inactive ferryl ions (FeO^{2+}), resulting in the deactivation of the catalyst, and (ii) the metal ions converted to metal hydroxide complexes^{8,43,44}. Figure 4C

illustrates the effect of the deposition potential on peak currents of Cd^{2+} and Pb^{2+} detection within the range from -1.6 to -1.0 V. It can be observed that the peak currents increased rapidly as the potential shifted from -1.6 to -1.3 V and then slowed down abruptly after having overtaken the potential -1.3 V. Therefore, -1.3 V was used as the suitable deposition potential with the highest current signal. This trend could be explained by the fact that the Cd^{2+} and Pb^{2+} ions were reduced upon the deposition potential raised to more negative values, however, as the deposition potential overcame the threshold value, the peak currents decreased due to the electrochemical evolution of hydrogen ions. And finally, the influence of the deposition time. Figure 4D exhibits the effect of the applied accumulation time on the sensitivity for Cd^{2+} and Pb^{2+} detection. As expected, when the accumulation or deposition time of the target metal ion was extended from 60 to 300 s, the peak currents greatly influenced and increased linearly until equilibrium was reached. Indeed, the current peaks for both metal ions have increased gradually up to 200 s, and beyond this time frame, they began to increase slightly until became steady. This steady trend is likely due to an oversaturation on the electrode surface caused by the huge amount of the target analytes^{18,45}. Hence, 200 s was chosen to be the optimized deposition time for the following experiments.

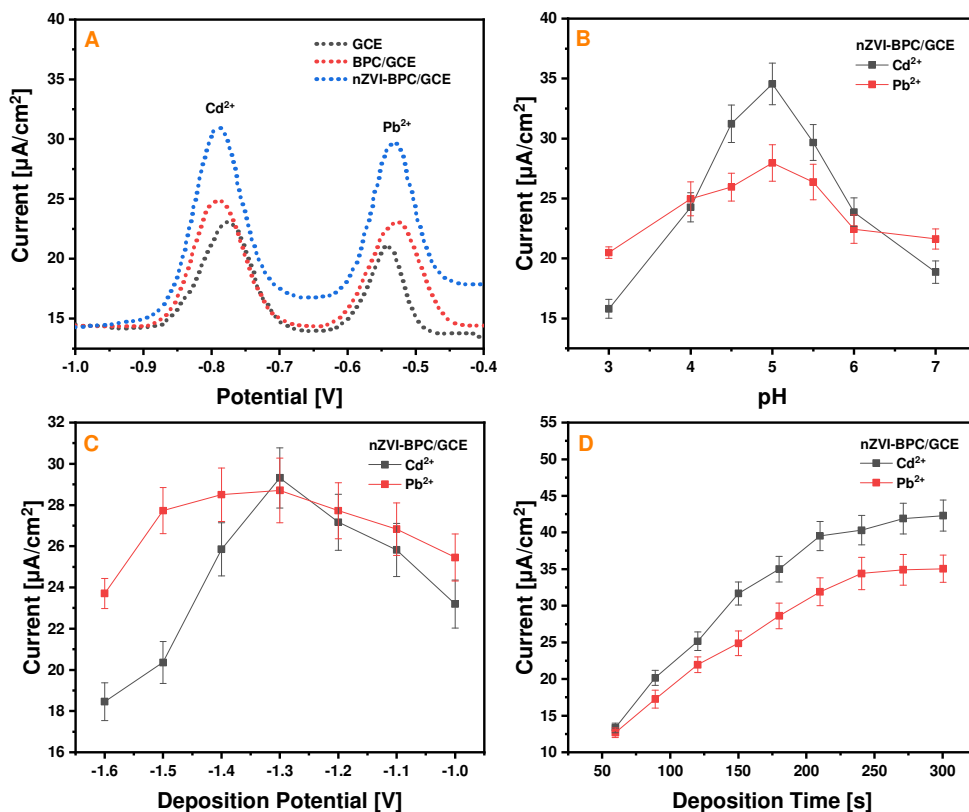
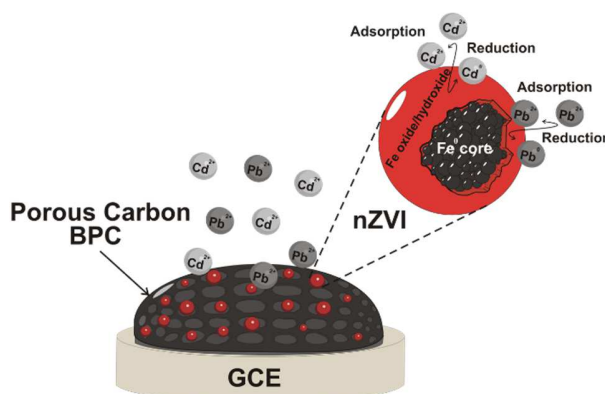


Figure 4. (A) SWSV of GCE bare, BPC/GCE, and nZVI-BPC/GCE, (B) plots of peak currents vs. pH solution, (C) plots of peak currents vs. deposition potential, and (D) plots of peak currents vs. deposition time of 50 $\mu\text{g}/\text{L}$ Cd^{2+} and Pb^{2+} ions in 0.1 M ABS.

Scheme 3. Mechanism of Cd^{2+} and Pb^{2+} assessment at nZVI-BPC/GCE surface.



3.3.2. Cd^{2+} and Pb^{2+} detection assays: calibration plots

Under the previous optimized experimental parameters, the quantitative determination for the simultaneous detection of Cd^{2+} and Pb^{2+} on the developed nZVI-BPC/GCE was monitored using the SWSV technique at the concentration range from 50 to 2 $\mu\text{g/L}$ in 0.1 M ABS (pH 5). Figure 5 shows the sensorgrams and the corresponding calibration curves. As demonstrated in Figure 5A, the current response of both Cd^{2+} and Pb^{2+} decreased proportionally as decreasing concentrations of the target metal ions. Hence, the peak current and the concentration of the Cd^{2+} and Pb^{2+} ions exhibit an appropriate linear relationship. Figure 5B reveals the linear plotting of the peak current against the corresponding metal ion concentration. The resulting fit of the calibration plots showed a strong correlation with CODs of 0.9919 and 0.9912 for Cd^{2+} and Pb^{2+} , respectively. The data supplied by the linear regression was then used to compute the quantitative parameters, such as limit of detection and sensitivity. Table S3 summarizes these parameters. As seen, the developed sensor possesses satisfactory detection limits ($LOD=3S_d/Slope$, where S_d is the standard deviation of the blank signal⁴⁶) of 0.1926 $\mu\text{g/L}$ for the Cd ion and 0.2082 $\mu\text{g/L}$ for the Pb ion with sensitivity values of 0.2336 and 0.2160 $\mu\text{A}/\mu\text{g}$, respectively, which were beyond the cutoff level recommended by the WHO (3 $\mu\text{g/L}$ for Cd^{2+} and 10 $\mu\text{g/L}$ for Pb^{2+}) in healthy drinking water⁴⁷. These significant achievements could be attributed to the intrinsic porous nature, efficient adsorptivity, and improved electrocatalytic ability of the nZVI-BPC nanocomposite.

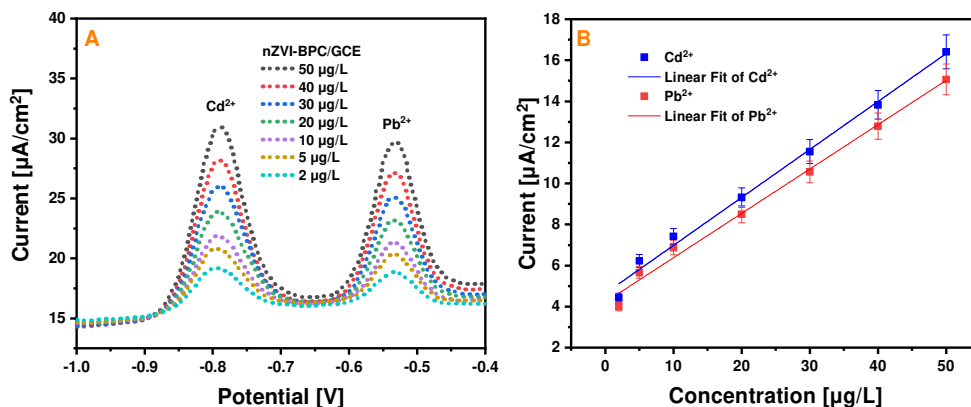


Figure 5. (A) Square-wave stripping voltammograms of the nZVI-BPC/GCE and (B) the respective calibration plots for the simultaneous detection of Cd²⁺ and Pb²⁺ ions at various concentrations (2–50 µg/L) in 0.1 M ABS (pH 5).

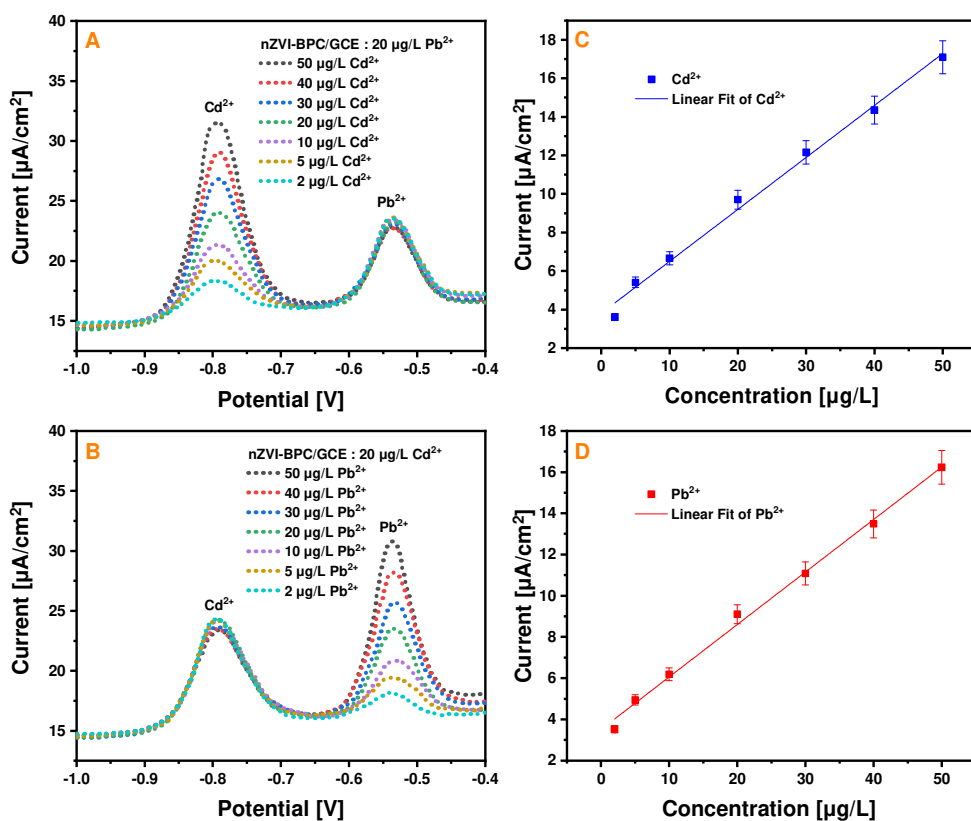


Figure 6. (A,B) Square-wave stripping voltammograms of the nZVI-BPC/GCE and (B,C) the respective calibration plots for the individual detection of Cd²⁺ and Pb²⁺ ions at various concentrations (2–50 µg/L) under the influence of 20 µg/L Cd²⁺ and/or Pb²⁺ in 0.1 M ABS (pH 5).

To investigate whether the simultaneous presence of Cd^{2+} and Pb^{2+} influences the individual analysis in each, the mutual interference between Cd^{2+} and Pb^{2+} for simultaneous detection was also examined in the same above-mentioned experimental parameters (Figure 6). Figure 6A shows the SWSV signals of Cd^{2+} over the varying concentration range from 50 to 2 $\mu\text{g/L}$ while keeping the Pb^{2+} concentration at 20 $\mu\text{g/L}$. It showed that the peak currents of Cd^{2+} decreased linearly in the range from 50 to 2 $\mu\text{g/L}$ while its counterpart of Pb^{2+} remain undisturbed. Likewise, the selective analysis of Pb^{2+} under the influence of 20 $\mu\text{g/L}$ Cd^{2+} was also carried out in the varied concentration range of 50–2 $\mu\text{g/L}$. A similar conclusion may be inferred, the current responses of Pb^{2+} decreased linearly upon decreasing its concentrations, while the peak current intensities of Cd^{2+} were practically unaffected (Figure 6B). Figure 6C and 6D present the corresponding calibration plots of Cd^{2+} and Pb^{2+} , respectively, in the competitive system. Both plots showed that the peak current intensity has a linear dependence on the ion concentration with a correlation of determination of 0.9928 for Cd^{2+} and 0.9954 for Pb^{2+} . Accordingly, the achieved sensitivities and detection limits data obtained from individual detection of Cd^{2+} and Pb^{2+} ions are tabulated and compared with those extracted from binary detection, as shown in Table S3. They are comparable to those obtained in simultaneous analysis, indicating the high selectivity of the nZVI-BPC/GCE.

3.3.3. Comparison of analytical performances with other relevant works

In order to estimate the analytical performances of the actual sensor, formerly relevant sensors already published in the literature and covering the simultaneous detection of Cd^{2+} and Pb^{2+} are compared. Table 1 enumerates the performances in terms of detection limit and linear dynamic range based on diverse analysis methods and electrode materials. Comparing the results enumerated in Table 1 shows how sensitive the designed electrode is towards the detection of Cd^{2+} and Pb^{2+} ions. The competitiveness of this sensor is obvious; it offers superior performance in terms of detection limit, sensitivity, and linear working range, which make it appreciated precisely for this kind of test. Owing to the synergy between the carbon substrate and zero-valent iron nanoparticles, the hierarchically porous framework provided by BPC acts as rigid support that provides a large number of loading sites for nZVI particles and can effectively inhibit their aggregation, which is beneficial to enhance the current response. Moreover, the strong adsorption ability and the excellent electrocatalytic activity of the nZVI ensure a highly active surface in electrochemical reactions and thus facilitate the reduction of Pb^{2+} and Cd^{2+} more easily. Therefore, this sensor may help analyze freshly water samples and sort out the overall and ongoing condition of the water. It is also worth noting that the proposed sensor is cheap and easy to fabricate.

Table 1. Comparison performances of the present sensor with reported studies.

	Technique	Material	Linear range	LOD	Reference
Metal ions: Cd ²⁺ and Pb ²⁺	SWASV	Pencil-lead carbon	2.0–24 µg/L 2.0–24 µg/L	0.4 µg/L 0.3 µg/L	48
	SWASV	Bi/ERGNO/SPE	1.0–60 µg/L 10–80 µg/L	0.5 µg/L 0.8 µg/L	49
	SWASV	Bi/Nafion/PPy/MES/GCE	0.05–35 g/L 0.1–25 g/L	0.03 g/L 0.04 g/L	50
	SWASV	BONPs-IL-CPE	3.0–30 µg/L 3.0–30 µg/L	0.15 µg/L 0.21 µg/L	51
	SWASV	Sb-MWCNT	10–60 µg/L 10–60 µg/L	0.65 µg/L 0.77 µg/L	52
	SWASV	BiNPs	1.0–100 µg/L 1.0–100 µg/L	0.65 µg/L 0.81 µg/L	53
	SWSV	BiNPs/SPCE	10–100 µg/L 10–100 µg/L	5.0 µg/L 2.0 µg/L	54
	DPSV	Bi/Au	10–80 µg/L 10–80 µg/L	0.7 µg/L 1.2 µg/L	55
	SWASV	Ce-Z	50–500 µg/L 50–500 µg/L	0.07 µg/L 0.46 µg/L	56
	SWASV	BiOCl powder in CPE	10–450 µg/L 10–400 µg/L	0.42 µg/L 0.76 µg/L	57
	DPV	r-CeO ₂ /EG/GCE	5.0–600 µg/L 5.0–600 µg/L	0.39 µg/L 0.21 µg/L	58
	SWASV	CUiO-66/Bi/GCE	10–50 µg/L 10–50 µg/L	1.16 µg/L 1.14 µg/L	59
	SWASV	MoS ₂ -RGO/Nafion/GCE	2.2–112.4 µg/L 4.1–207.2 µg/L	0.59 µg/L 0.13 µg/L	60
	SWSV	nZVI-BPC/GCE	2.0–50 µg/L 2.0–50 µg/L	0.19 µg/L 0.20 µg/L	Current work

SWASV: square-wave anodic stripping voltammetry; DPSV: differential pulse stripping voltammetry; PPy: polypyrrole; MES: overoxidized 2-mercaptoethanesulfonate-tethered; BONPs-IL-CPE: bismuth oxide nanoparticles and ionic liquid modified carbon paste electrode; MWCNT: multiwalled carbon nanotubes; Z: zeolite; EG: expanded graphite; CUiO-66: metal-organic framework material; RGO: reduced graphene oxide; SPCE: screen-printed carbon electrode; ERGNO: electrochemically reduced graphene oxide film; SPE: screen-printed electrode; CPE: carbon paste electrode.

3.3.4. Sensor selectivity, reproducibility, and stability

Selectivity of the developed sensor for simultaneous detection of Cd²⁺ and Pb²⁺ ions during analysis is a paramount parameter to evaluate the specificity of the nZVI-BPC/GCE for the target analyte. Hence, interferences arising from foreign electroactive inorganic ions (K⁺, Na⁺, Zn²⁺, Mg²⁺, Ca²⁺, Fe²⁺, and Cu²⁺) and organic compounds such as pesticides (atrazine and metolachlor) expected to co-exist in an aquatic environment were investigated under the same optimum experimental conditions, described previously. Typically, a 40-fold tolerate ratio of the interferent ion and 10-fold higher concentration for the interferent pesticide were spiked into 0.1 M ABS (pH 5) containing 20 µg/L Cd²⁺ and Pb²⁺ ions. The degree of interference is expressed in terms of relative standard deviation (RSD) of the peak currents of Cd²⁺ and Pb²⁺ (Table S4). As

reported in Table S4, most of the interfering species exhibit a low degree of interference with the deviations are below or around 5%, suggesting that no obvious influence has occurred on the current responses of Cd^{2+} and Pb^{2+} ions. Only atrazine and metolachlor caused a relatively higher deviation in the signal (slightly above 5%), which may be attributed to the high affinity of nZVI for chlorinated pesticides. Commonly, an active ingredient is considered as a potential interferent when its influence on the peak current of the target analyte reaches up to $\pm 5\%$ deviation⁵⁴. Anyway, the obtained results demonstrate the high intransigence of the nZVI-BPC/GCE to interference, which predicts outstanding measuring accuracy for the simultaneous detection of Cd^{2+} and Pb^{2+} ions in freshwater.

The reproducibility and stability of the nZVI-BPC/GCE (Figure S2) have been also assessed in the same way as that described above. A series of 10 repetitive measurements (Figure S2A) were carried out at the same modified electrode for simultaneous detection of 20 $\mu\text{g/L}$ Cd^{2+} and Pb^{2+} ions in 0.1 M ABS (pH 5). Practically, there has been no noticeable change in the current intensities of the metal ions as the relative's standard deviation (RSD, $n = 10$) values are about 1.12% for Cd^{2+} and 1.33% for Pb^{2+} , respectively. The stability of nZVI-BPC/GCE was checked while storing the working electrode at 4° C and monitoring the variation of the peak current of 20 $\mu\text{g/L}$ of the Cd^{2+} and Pb^{2+} ions at regular intervals (every 5 days) over 1 month (Figure S2B). Data showed that the response signals for Cd^{2+} and Pb^{2+} detection retained more than 90% of its initial response with 94.43% for Cd^{2+} and 92.7% for Pb^{2+} upon 30 days. Nevertheless, these results confirm the ability of the proposed sensor to withstand long-term operational stability and excellent reproducibility.

3.3.5. Realistic sample tests

To access the practical application of the developed sensor in routine analysis, the nZVI-BPC/GCE was run to detect simultaneously Cd^{2+} and Pb^{2+} in a drinking tap water sample. In short, Cd^{2+} and Pb^{2+} at concentrations of 10, 5.0, and 2 $\mu\text{g/L}$ were spiked into drinking water samples, respectively, and analyzed using the stripping SWSV method under the same conditions. Accordingly, results deduced from sensorgrams are depicted in Table S5 taking into account the recovery percentage for the spiked concentration. As shown in Table S5, the recovery rates were ranging between 96% and 104 % with RSD values between 2.98% and 5.76%, suggesting the high potential of the nZVI-BPC/GCE for accurate and reliable determination of Cd^{2+} and Pb^{2+} in fresh water and therefore qualifies the present sensor to monitor water quality.

4. Conclusions

In summary, a working nZVI-BPC/GCE modified electrode was developed and subsequently used for the simultaneous detection of Cd^{2+} and Pb^{2+} ions. Firstly, the nZVI-BPC nanocomposite has

been prepared following the liquid-phase reduction and impregnation methods. The characteristics of the physico-chemical and electrochemical behavior of nZVI-BPC were studied using various techniques such as XRD, FT-IR, Raman, XPS, TEM, nitrogen adsorption/desorption isotherm, CV, and EIS. The nZVI particles were successfully dispersed throughout the surface of the BPC with typically interconnected micro-and mesoporous structures. The as-synthesized nZVI-BPC was then employed as a bulk material to modify GCE and applied for the simultaneous detections of Cd^{2+} and Pb^{2+} using stripping voltammetry (SWSV). Due to the outstanding properties of the nZVI-BPC nanocomposite, the fabricated sensor exhibited a high and sharp stripping peak current for the target metal ions and demonstrated sound sensitivity, low detection limit, high selectivity, good reproducibility, and practical stability. In addition, this sensor has proved the enormous potential for analysis in real sample assays, which therefore could expand the scope of the device from monitoring water quality to ensuring food safety.

Associated content

Supporting information

Figure S1. Textural properties of BPC matrix and nZVI-BPC nanocomposite: (A) N_2 sorption isotherms and (B) pore size distribution plots; **Figure S2.** (A) Reproducibility and (B) stability measurements of the sensor; **Table S1.** Textural parameters of BPC matrix and nZVI-BPC nanocomposite; **Table S2.** Anodic and cathodic peaks were obtained from CV curves and charge transfer resistances were determined using EIS Nyquist plots of GCE bare, BPC/GCE, and nZVI-BPC/GCE; **Table S3.** Analytical performances for simultaneous (binary) and individual (single) detection of Cd^{2+} and Pb^{2+} ; **Table S4.** Study of potential interfering ions; **Table S5.** Simultaneous determination of Cd^{2+} and Pb^{2+} ions in drinking water samples.

Author information

Corresponding author

Mohamed Amine Djebbi – Laboratory of Ressources, Materials & Ecosystem (RME), University of Carthage, Faculty of Sciences of Bizerte, Zarzouna, 7021, Tunisia; orcid.org/0000-0002-7237-3557; Email: med-djebbi@hotmail.fr, mohammed-amine.djebbi@inrae.fr

Authors

Lakhdar Allagui – Laboratory of Ressources, Materials & Ecosystem (RME), University of Carthage, Faculty of Sciences of Bizerte, Zarzouna, 7021, Tunisia; orcid.org/; Email: lakhdar.allagui@gmail.com

Mohamed Slim El Ayachi – Laboratory of Ressources, Materials & Ecosystem (RME), University of Carthage, Faculty of Sciences of Bizerte, Zarzouna, 7021, Tunisia; orcid.org/0000-0002-3814-2480; Email: e.mohamedslim@yahoo.fr

Saber Boubakri – National Institute for Research and Physico-chemical Analysis, BiotechPole Sidi-Thabet, Ariana, 2020, Tunisia; orcid.org/0000-0001-6141-4854; Email: mohamedsabrito@gmail.com

Nicole Jaffrezic-Renault – Institute of Analytical Sciences, University of Lyon, 5 rue de la Doua, Villeurbanne, 69100, France; orcid.org/0000-0003-1354-9273; Email: nicole.jaffrezic@univ-lyon1.fr

Philippe Namour – INRAE, UR RiverLy, Centre de Lyon-Villeurbanne, 5 rue de la Doua CS 20244, Villeurbanne, 69625, France; orcid.org/0000-0003-4252-4913; Email: philippe.namour@inrae.fr

Abdesslem Ben Haj Amara – Laboratory of Ressources, Materials & Ecosystem (RME), University of Carthage, Faculty of Sciences of Bizerte, Zarzouna, 7021, Tunisia; orcid.org/0000-0002-2531-0254; Email: abdesslem.bha@gmail.com

Funding

This research received no specific grant from any funding agency in the public, commercial, or not-for-profit sectors.

Notes

The authors declare no competing financial interest.

Acknowledgment

The authors would like to acknowledge all those who contributed their time and resources to the development of this work.

References

- [1]. Gaur, N.; Flora, G.; Yadav, M.; Tiwari, A. A review with recent advancements on bioremediation-based abolition of heavy metals. *Environ. Sci.: Processes Impacts* **2014**, *16*, 180–193.
- [2]. Nik Abd. Rahman, N. N.; Shahadat, M.; Won, C. A.; Omar, F. M. FTIR study and bioadsorption kinetics of bioadsorbent for the analysis of metal pollutants. *RSC Adv.* **2014**, *4*, 58156–58163.
- [3]. Wang, Y.; Ye, G.; Chen, H.; Hu, X.; Niu, Z.; Ma, S. Functionalized metal–organic framework as a new platform for efficient and selective removal of cadmium(II) from aqueous solution. *J. Mater. Chem. A* **2015**, *3*, 15292–15298.
- [4]. Järup, L.; Hazards of heavy metal contamination. *Br. Med. Bull.* **2013**, *68*, 167–182.

- [5]. Boubakri, S.; Djebbi, M. A.; Bouaziz, Z.; Namour, P.; Ben Haj Amara, A.; Ghorbel-Abid, I.; Kalfat, R. Nanoscale zero-valent iron functionalized *Posidonia oceanica* marine biomass for heavy metal removal from water. *Environ. Sci. Pollut. Res.* **2017**, *24*, 27879–27896.
- [6]. Zhang, T.; Jin, H.; Fang, Y.; Guan, J. B.; Ma, S. J.; Pan, Y.; Zhang, M.; Zhu, H.; Liu, X. D.; Du, M. L. Detection of trace Cd^{2+} , Pb^{2+} and Cu^{2+} ions via porous activated carbon supported palladium nanoparticles modified electrodes using SWASV. *Materials Chemistry and Physics* **2019**, *225*, 433–442.
- [7]. Liu, Y.; Li, T.; Ling, C.; Chen, Z.; Deng, Y.; He, N. Electrochemical sensor for Cd^{2+} and Pb^{2+} detection based on nano-porous pseudo carbon paste electrode. *Chinese Chemical Letters* **2019**, *30*, 2211–2215.
- [8]. Zhu, X.; Liu, B.; Chen, S.; Wu, L.; Yang, J.; Liang, S.; Xiao, K.; Hu, J.; Hou, H. Ultrasensitive and simultaneous electrochemical determination of Pb^{2+} and Cd^{2+} based on biomass derived lotus root-like hierarchical porous carbon/bismuth composite. *Journal of The Electrochemical Society* **2020**, *167*, 087505.
- [9]. Seenivasan, R.; Chang, W.-J.; Gunasekaran, S. Highly sensitive detection and removal of lead ions in water using cysteine-functionalized graphene oxide/polypyrrole nanocomposite film electrode. *ACS Appl. Mater. Interfaces* **2015**, *7*, 15935–15943.
- [10]. Kumar, S.; Nair, R. R.; Pillai, P. B.; Gupta, S. N.; Iyengar, M. A. R.; Sood, A. K. Graphene oxide– MnFe_2O_4 magnetic nanohybrids for efficient removal of lead and arsenic from water. *ACS Appl. Mater. Interfaces* **2014**, *6*, 17426–17436.
- [11]. World Health Organization. Guidelines for Drinking-Water Quality, 4th ed., **2011**. http://whqlibdoc.who.int/publications/2011/9789241548151_eng.pdf.
- [12]. Zhou, Z.; Wang, C.; Liu, H.; Huang, Q.; Wang, M.; Lei, Y. Cadmium induced cell apoptosis, DNA damage, decreased DNA repair capacity, and genomic instability during malignant transformation of human bronchial epithelial cells. *Int. J. Med. Sci.* **2013**, *10*, 1485–1496.
- [13]. Ihsanullah, Al-Khaldi, F. A.; Abusharkh, B.; Khaled, M.; Atieh, M. A.; Nasser, M. S.; Laoui, T.; Saleh, T. A.; Agarwal, S.; Tyagi, I. Adsorptive removal of cadmium(II) ions from liquid phase using acid modified carbon-based adsorbents. *J. Mol. Liq.* **2015**, *204*, 255–263.
- [14]. Liu, C.; Zhang, D.; Zhao, L.; Lu, X.; Zhang, P.; He, S.; Hu, G.; Tang, X. Synthesis of a thiacalix[4]arenetetrasulfonate functionalized reduced graphene oxide adsorbent for the removal of lead(II) and cadmium(II) from aqueous solutions. *RSC Adv.* **2016**, *6*, 113352–113365.
- [15]. Veerakumar, P.; Veeramani, V.; Chen, S.-M.; Madhu, R.; Liu, S.-B. Palladium nanoparticle incorporated porous activated carbon: electrochemical detection of toxic metal ions. *ACS Appl. Mater. Interfaces* **2016**, *8*, 1319–1326.

- [16]. Vega-Figueroa, K.; Santillan, J.; Ortiz-Gomez, V.; Ortiz-Quiles, E. O.; Quinones-Colon, B. A.; Castilla-Casadiago, D. A.; Almodovar, J.; Bayro, M. J.; Rodríguez-Martínez, J. A.; Nicolau, E. Aptamer-based impedimetric assay of arsenite in water: Interfacial properties and performance. *ACS Omega* **2018**, 3, 1437–1444.
- [17]. Li, S.; Zhang, C.; Wang, S.; Liu, Q.; Feng, H.; Ma, X.; Guo, J. Electrochemical microfluidics techniques for heavy metal ion detection. *Analyst* **2018**, 143, 4230–4246.
- [18]. Shirley, T. P.; Remuel, I. M. V.; Marissa, G. N.; Katja, T. P.; Michelle, T. N. Highly sensitive determination of heavy metals in water prior to and after remediation using *Citrofortunella Microcarpa*. *Sci. Rep.* **2021**, 11, 1394.
- [19]. Phetsang, S.; Khwannimit, D.; Rattanakit, P.; Chanlek, N.; Kidkhunthod, P.; Mungkornasawakul, P.; Jakmune, J.; Ounnunkad, K. A redox Cu(II)-graphene oxide modified screen printed carbon electrode as a cost-effective and versatile sensing platform for electrochemical label-free immunosensor and non-enzymatic glucose sensor. *Front. Chem.* **2021**, 9, 671173.
- [20]. Khristunova, E.; Dorozhko, E.; Korotkova, E.; Kratochvil, B.; Vyskocil, V.; Barek, J. Label-free electrochemical biosensors for the determination of Flaviviruses: Dengue, Zika, and Japanese Encephalitis. *Sensors* **2020**, 20, 4600.
- [21]. Palisoc, S.; Causing, A. M.; Natividad, M. Gold nanoparticle /hexaammineruthenium/Nafion® modified glassy carbon electrodes for trace heavy metal detection in commercial hair dyes. *Anal. Methods* **2017**, 9, 4240–4246.
- [22]. Yu, X. Y.; Meng, Q. Q.; Luo, T.; Jia, Y.; Sun, B.; Li, Q. X.; Liu, J. H.; Huang, X. J. Facet-dependent electrochemical properties of Co₃O₄ nanocrystals toward heavy metal ions. *Sci. Rep.* **2013**, 3, 2886.
- [23]. Tang, Y.; Cheng, W. Nanoparticle-modified electrode with size- and shape-dependent electrocatalytic activities. *Langmuir* **2013**, 29, 3125–3132.
- [24]. Veerakumar, P.; Madhu, R.; Chen, S. M.; Hung, C. T.; Tang, P. H.; Wang, C. B.; Liu, S. B. Porous carbon-modified electrodes as highly selective and sensitive sensors for detection of dopamine. *Analyst* **2014**, 139, 4994–5000.
- [25]. Palisoc, S. T.; Natividad, M. T.; De Jesus, N.; Carlos, J. Highly sensitive AgNP/MWCNT/Nafion modified GCE-based sensor for the determination of heavy metals in organic and non-organic vegetables. *Sci. Rep.* **2018**, 8, 17445.
- [26]. Ponder, S. M.; Darab, J. G.; Mallouk, T. E. Remediation of Cr (VI) and Pb (II) aqueous solutions using nanoscale zero-valent iron. *Environ. Sci. Technol.* **2000**, 34, 2564–2569.
- [27]. Yidong Z.; Xiangxue W.; Ayub K.; Pengyi W.; Yunhai L.; Ahmed A.; Tasawar H.; Xiangke W. Environmental remediation and application of nanoscale zerovalent iron and its

- composites for the removal of heavy metal ions: A review. *Environ. Sci. Technol.* **2016**, 50, 7290–7304.
- [28]. Ling, L.; Tang, C.; Zhang, W.-X. Visualization of silver nanoparticle formation on nanoscale zero-valent iron. *Environ. Sci. Technol. Lett.* **2018**, 5, 520–525.
- [29]. Greenlee, L. F.; Torrey, J. D.; Amaro, R. L.; Shaw, J. M. Kinetics of zero valent iron nanoparticle oxidation in oxygenated water. *Environ. Sci. Technol.* **2012**, 46, 12913–12920.
- [30]. Deng, J.; Li, M.; Wang, Y. Biomass-derived carbon: synthesis and applications in energy storage and conversion. *Green Chem.* **2016**, 18, 4824–4854.
- [31]. Varma, R. S. Biomass-derived renewable carbonaceous materials for sustainable chemical and environmental applications. *ACS Sustainable Chem. Eng.* **2019**, 7, 6458–6470.
- [32]. Liu, X.; Lai, D.; Wang, Y. Performance of Pb(II) removal by an activated carbon supported nanoscale zero-valent iron composite at ultralow iron content. *Journal of Hazardous Materials* **2019**, 361, 37–48.
- [33]. Liu, X.; Wang, Y. Activated carbon supported nanoscale zero-valent iron composite: Aspects of surface structure and composition. *Materials Chemistry and Physics* **2019**, 222, 369–376.
- [34]. Chen, R.; Wang, P.; Li, M.; Tian, F.; Xiao, J.; Fu, X.; Ding, C.; Shi, Y. Removal of Cr(VI) by magnetic Fe/C crosslinked nanoparticle for water purification: rapid contaminant removal property and mechanism of action. *Water. Sci. Technol.* **2018**, 78, 2171–2182.
- [35]. Song, Y.; Wang, L.; Lv, B.; Chang, G.; Jiao, W.; Liu, Y. Removal of trace Cr(VI) from aqueous solution by porous activated carbon balls supported by nanoscale zero-valent iron composites. *Environ. Sci. and Pollut. Res.* **2020**, 27, 7015–7024.
- [36]. Djebbi, M. A.; Boubakri, S.; Braiek, M.; Jaffrezic-Renault, N.; Namour, P.; Ben Haj Amara, A. Chlorpromazine electro-oxidation at BDD electrode modified with nZVI nanoparticles impregnated NiAl LDH. *Electroanalysis* **2020**, 32, 1186–1197.
- [37]. Djebbi, M. A.; Braiek, M.; Namour, P.; Jaffrezic-Renault, N.; Ben Haj Amara, A. Layered double hydroxide materials coated carbon electrode: New challenge to future electrochemical power devices. *App. Surf. Sci.* **2016**, 386, 352–363.
- [38]. Hu, Y.; Xie, K.; Wang, H.; Yuan, C.; Cao, B.; Qian, L.; Wang, S.; Zafar, F. F.; Ding, K.; Wang, Q. Preparation and property of N-doped porous carbon material by one-step pyrolysis of protein-rich algal biomass. *Journal of Analytical and Applied Pyrolysis* **2021**, 157, 105221.
- [39]. Tang, A. J.; Wang, T.; Pan, X.; Sun, X.; Fan, X.; Guo, Y.; Xue, H.; He, J. Synthesis and electrochemical characterization of N-Doped partially graphitized ordered mesoporous carbon–Co composite. *J. Phys. Chem. C* **2013**, 117, 16896–16906.

- [40]. Jiang, Y.; Cheng, G.; He, Z.; Chen, J.; Li, Y.; Zhu, J.; Meng, W.; Zhou, H.; Dai, L.; Wang, L. Biomass-derived porous graphitic carbon with excellent electrocatalytic performances for vanadium redox reactions. *Journal of The Electrochemical Society* **2019**, 166, 3918–3926.
- [41]. Djebbi, M.A.; Boubakri, S.; Braiek, M.; Jaffrezic-Renault, N.; Namour, P.; Ben Haj Amara, A. High performance non-Enzymatic electrochemical lactate sensor based on ZnAl layered double hydroxide nanosheets supported gold nanoparticles, *Journal of The Electrochemical Society* **2021**, 168, 057529.
- [42]. Ramli, N. I.; Ismail, N. A. B.; Abd-Wahab, F.; Wan Salim, W. W. A.; Cyclic voltammetry and electrical impedance spectroscopy of electrodes modified with PEDOT:PSS-reduced graphene oxide composite. *Intechopen* **2018**, 75–84.
- [43]. Yang, B.; Tian, Z.; Zhang, L.; Guo, Y.; Yan, S. Enhanced heterogeneous Fenton degradation of Methylene Blue by nanoscale zero valent iron (nZVI) assembled on magnetic Fe₃O₄/reduced graphene oxide. *Journal of Water Process Engineering* **2015**, 5, 101–111.
- [44]. Bao, T.; Jin, J.; Damtie, M. M.; Wu, K.; Yu, Z. M.; Wang, L.; Chen, J.; Zhang, Y.; Frost, R. L. Green synthesis and application of nanoscale zero-valent iron/rectorite composite material for P-chlorophenol degradation via heterogeneous Fenton reaction. *Journal of Saudi Chemical Society* **2019**, 23, 864–878.
- [45]. Baghayeri, M.; Amiri, A.; Maleki, B.; Alizadeh, Z.; Reiser, O. A simple approach for simultaneous detection of cadmium (II) and lead (II) based on glutathione coated magnetic nanoparticles as a highly selective electrochemical probe. *Sens. Actuators B Chem.* **2018**, 273, 1442–1450.
- [46]. Mocak, J.; Bond, A. M.; Mitchell, S.; Scollary, G. A statistical overview of standard (IUPAC and ACS) and new procedures for determining the limits of detection and quantification: Application to voltammetric and stripping techniques. *Pure Appl. Chem.* **1997**, 69, 297–328.
- [47]. Martín-Yerga, D.; Álvarez-Martos, I.; Blanco-Lopez, M. C.; Henry, C. S.; Fernández-Abedul, M.T. Point-of-need simultaneous electrochemical detection of lead and cadmium using low-cost stencil-printed transparency electrodes. *Anal. Chim. Acta* **2017**, 981, 24–33.
- [48]. Demetriades, D.; Economou, A.; Voulgaropoulos, A. A study of pencil-lead bismuth-film electrodes for the determination of trace metals by anodic stripping voltammetry. *Anal. Chim. Acta* **2004**, 519, 167–172.
- [49]. Ping, J.; Wang, Y.; Wu, J.; Ying, Y. Development of an electrochemically reduced graphene oxide modified disposable bismuth film electrode and its application for stripping analysis of heavy metals in milk. *Food Chemistry* **2013**, 151, 65–71.
- [50]. Chen, L.; Li, Z.; Meng, Y.; Zhang, P.; Su, Z.; Liu, Y.; Huang, Y.; Zhou, Y.; Xie, Q.; Yao, S. Sensitive square wave anodic stripping voltammetric determination of Cd²⁺ and Pb²⁺ ions

at Bi/Nafion/overoxidized 2-mercaptoethanesulfonate-tethered polypyrrole/glassy carbon electrode. *Sens. Actuators B* **2014**, 191, 94–101.

- [51]. Chaudhari, K. N.; Song, M. Y.; Yu, J. S. Transforming hair into heteroatom-doped carbon with high surface area. *Small* **2014**, 10, 2625–2636.
- [52]. Ashrafi, A. M.; Cerovac, S.; Mudrić, S.; Guzsány, V.; Husáková, L.; Urbanoá, I.; Vytřas, K. Antimony nanoparticle-multiwalled carbon nanotubes composite immobilized at carbon paste electrode for determination of trace heavy metals. *Sens. Actuat. B Chem.* **2014**, 191, 320.
- [53]. Niu, P. F.; Fernández-Sánchez, C.; Gich, M.; Ayora, C.; Roig, A. Electroanalytical assessment of heavy metals in waters with bismuth nanoparticle-porous carbon paste electrodes. *Electrochim. Acta* **2015**, 165, 155.
- [54]. Cadevall, M.; Ros, J.; Merkoč, A. Bismuth nanoparticles integration into heavy metal electrochemical stripping sensor. *Electrophoresis* **2015**, 36, 1872–1879.
- [55]. Zhang, W.; Zhang, H.; Williams, S. E.; Zhou, A. H. Microfabricated three-electrode on-chip PDMS device with a vibration motor for stripping voltammetric detection of heavy metal ions. *Talanta* **2015**, 132, 321–326.
- [56]. Kawde, A.; Ismail, A.; Al-Betra, A. R.; Muraza, O. Novel Ce-incorporated zeolite modified carbon paste electrode for simultaneous trace electroanalysis of lead and cadmium. *Micropor. Mesopor. Mater.* **2017**, 243, 1.
- [57]. Liu, L.; Yu, C.; Zhang, X.; Ma, H.; Ma, C.; Fu, Y.; Dong, X. Carbon paste electrode modified with bismuth oxychloride as a sensor for the determination of Pb^{2+} and Cd^{2+} . *Int. J. Electrochem. Sci.* **2019**, 14, 4469–4482.
- [58]. Huang, W.; Zhang, Y.; Li, Y.; Zeng, T.; Wan, Q.; Yang, N. Morphology-controlled electrochemical sensing of environmental Cd^{2+} and Pb^{2+} ions on expanded graphite supported CeO_2 nanomaterials. *Analytica Chimica Acta* **2020**, 1126, 63–71.
- [59]. Ding, Y.; Wei, F.; Dong, C.; Li, J.; Zhang, C.; Han, X. UiO-66 based electrochemical sensor for simultaneous detection of Cd(II) and Pb(II). *Inorganic Chemistry Communications* **2021**, 131, 108785.
- [60]. Yin, J.; Chu, G.; Wang, Y.; Zhai, H.; Wang, B.; Sun, X.; Guo, Y.; Zhang, Y. Novel three-dimensional sensor for rapid detection of Pb(II) and Cd(II) in edible mushrooms. *Electroanalysis* **2021**, 33, 1370–1377.